Supporting Info for "Indistinguishable photons from deterministically integrated single quantum dots in heterogeneous GaAs/Si$_3$N$_4$ quantum photonic circuits"

Peter Schnauber,[†] Anshuman Singh,[‡,¶] Johannes Schall,[†] Suk In Park,[§] Jin Dong Song,[§] Sven Rodt,[†] Kartik Srinivasan,[‡,‖] Stephan Reitzenstein,[†] and Marcelo Davanco[*,‡]

†*Institute of Solid State Physics, Technische Universität Berlin, Berlin, Germany*

‡*National Institute of Standards and Technology, Gaithersburg, MD, USA*

¶*Maryland NanoCenter, University of Maryland, College Park, USA*

§*Center for Opto-Electronic Convergence Systems, Korea Institute of Science and Technology, Seoul, South Korea*

‖*Joint Quantum Institute, NIST/University of Maryland, College Park, USA*

E-mail: marcelo.davanco@nist.gov

I. Charging effects during fabrication

As can be seen from Fig. 2 b) and c) in the main text, some WGs show a downward-bent left-hand part. The WG bending amplitude correlates with the duration of the in-situ EBL process (stronger bending at later times during the 6 h in-situ EBL run). It also correlates with the size of the GaAs layer area around the device (stronger bending for devices closer to GaAs layer borders). Both effects hint that during the in-situ EBL run, charge continuously accumulates and at some point cannot be dissipated sufficiently anymore. This leads to a charge build-up in the mapping process that deviates the beam in the beginning of the patterning step. This effect can be reproduced in the post-fabrication mapping: Because no planar GaAs exists around the fabricated devices anymore, there is insufficient charge dissipation and the beam is deviated in the beginning of the post-fabrication mapping process, as can be seen in the simultaneously acquired SEM image in Fig. S1 a). Fig. S1 b) depicts an optical micrograph of the same WG device, showing that it is not bent. The beam shift is analogous to the deviations for devices fabricated late in the in-situ EBL run. In the post-fabrication maps Fig. 2 g) - i) in the main text, beam deviations at the GaAs devices were avoided by starting the map far enough away for the beam to stabilize before scanning the GaAs devices. As discussed in the main text, lower QD densities requiring lower beam currents, as well as a thinner SiO_2 layer and conductive polymers on top of the EBL resist are expected to significantly reduce charging in the future.

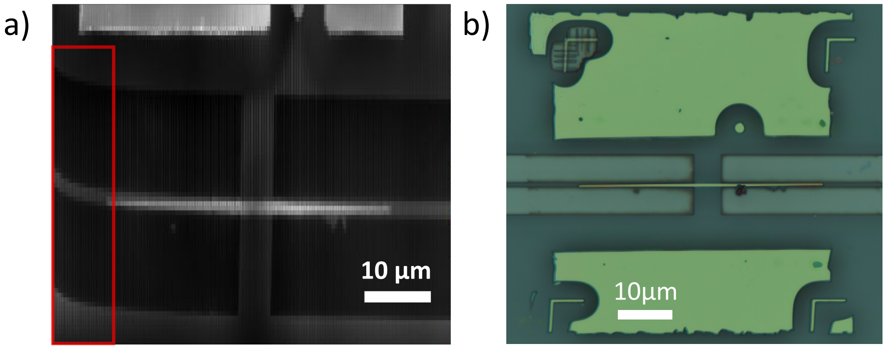

Figure S1: a) SEM image of device QD 1 taken during post-fabrication CL mapping. In the first few seconds of the mapping process, the beam is deviated by a charge build-up, before stabilizing for the rest of the map. b) False-color optical microscope image of the same device proving that device QD 1 consists of straight WGs.

II. GaAs waveguide taper pattern

The GaAs nanowaveguides, which host the InAs QD, are patterned using proximity-corrected grey-scale EBL. This is particularly important as the electron dose per pixel needed for cross-linking the resist increases by a factor of more than 4 at the taper tip, as compared to the taper center. Fig. S2 shows the target and the proximity-corrected pattern used to write the nanowaveguide that hosts QD 1-3. A close-up of the grey-scale pattern taper tip is also shown. The electron dose is encoded linearly in the 256 grey-scale steps.

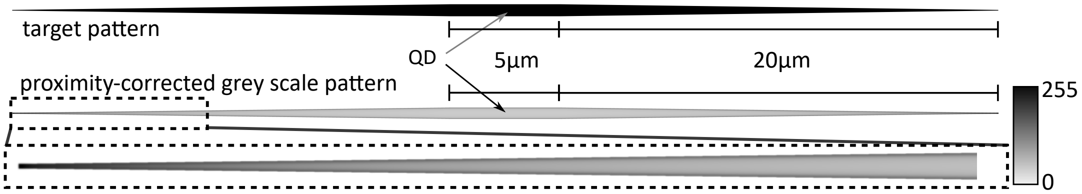

Figure S2: top: Target GaAs nanowaveguide pattern used to integrate QD 1-3. btm: Proximity-corrected grey-scale EBL pattern for in-situ EBL to manufacture the target pattern along with a close-up of the grey-scale taper-tip for better visualization of the grey scales.

III. Power-dependent emission red-shift

To investigate the red-shift of the $\approx 916.3\,\mathrm{nm}$ emission line under p-shell excitation, we assume a linear increase $T = T_0 + \eta\ P$ in temperature with excitation power P, starting from a base temperature of $T_0 = 7$ K, and fit this dependence with a Bose-Einstein phonon law[1,2] to the power-dependent peak positions $E_{\mathrm{QD}}(P)$, see Fig. 3 c) in the main text.

$$E_{\mathrm{QD}}(P) = E_{\mathrm{QD}}(0) - S\ E_{\mathrm{Ph}}\ \coth\left(\frac{E_{\mathrm{Ph}}}{2\ (T_0 + \eta\ P)\ k_{\mathrm{B}}}\right) \tag{1}$$

Here, $S = 0.5 \pm 0.1$ gives the phonon coupling strength, $E_{\mathrm{Ph}} = (1.71 \pm 0.06)\,\mathrm{meV}$ is the phonon energy and $\eta = (6700 \pm 1400)$ K/W is the power-temperature-coefficient (all uncertainties are standard errors). As can be seen from Fig. 3 c) in the main text, the model represents the data very well, hinting that the temperature increases linearly with excitation power. To further investigate, we take a temperature series of the $\approx 916.3\,\mathrm{nm}$ emission line, shown in Fig. S3 a). In this series, we measure the temperature within the cryostat cold finger and assume that it is equal to the actual GaAs nanowaveguide temperature, which is not directly measurable. We find that the emission energies measured in the temperature series, see Fig. S3 b), red-shift faster than predicted using the $T = T_0 + \eta\ P$ law. This means that a more elaborate model is needed to fully describe the thermal behaviour of our hybrid system. During the power series experiment, the excitation wavelength remained unchanged.

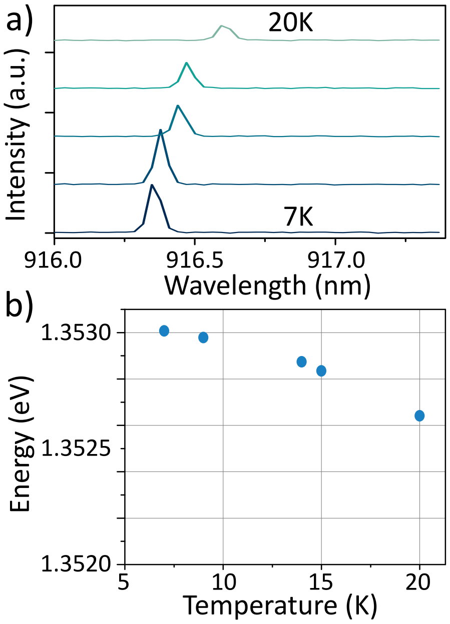

Figure S3: a) Temperature series taken at temperatures of 7 K, 9 K, 14 K, 15 K and 20 K. We added an arbitrary intensity offset in the spectra for better visualization. b) Peak energies from a) against cold-finger temperature.

IV. Upper bound estimate for the QD-waveguide and QD-lensed optical fiber coupling efficiency

To estimate the maximum expected coupling efficiency between QD 3 and the fundamental TE Si_3N_4 waveguide mode, we used Finite Difference Time Domain (FDTD) simulations of electric dipoles emitting in a hybrid waveguide/mode transformer that approximated the geometry observed in SEM. In this model, the GaAs, SiO_2 spacer and Si_3N_4 layers had a thickness of 190 nm, 100 nm and 250 nm, respectively. The straight section of the GaAs waveguide had a width of 620 nm and length of 5 µm, and the mode transformer was tapered down to a width of 100 nm over a length of 20 µm. The GaAs nanowaveguide and the underlying, 685 nm width Si_3N_4 waveguide were horizontally misaligned from each other by 44 nm. The FDTD simulations consisted of exciting the geometry with an electric dipole source located at the geometrical center of the GaAs nanowaveguide, and calculating the steady-state fields at a 916 nm wavelength, at the edges of the computational domain.

The simulation incorporated perfectly-matched layers to emulate open domains. The total emitted power of the dipole was obtained by integrating the steady-state Poynting vector over all of the computational domain boundaries. The power carried by the various guided modes supported by the GaAs and Si_3N_4 waveguides were obtained through overlap integrals with the steady-state field at the waveguides' cross-section. Simulations were performed for horizontally oriented dipole moments, either transversal (x-oriented) or longitudinal (z-oriented) to the GaAs nanowaveguide. Because we believe the $\approx 916.3\,\mathrm{nm}$ emission line of QD 3 to be from a charged exciton, which would have circularly polarized transitions, we have also simulated the case of a rotating dipole (the x- and z-components with a 90° phase between them).[3] However, because a transversal dipole tends to couple more efficiently to the fundamental TE-like GaAs mode, it yields a more conservative upper-bound estimate for the QD-Si_3N_4 waveguide coupling.

The 620 nm wide GaAs waveguide supports 7 guided modes at 916 nm, as shown in Fig. S4. The dipole emission is divided among such guided modes, as well as unguided, radiation or substrate modes. Figure S4 also shows the coupling ratios ($\beta_{x,y,z}$) for each guided mode, for the transverse (x), longitudinal (z), and rotating dipole (c) cases. The highest coupling ratio achievable in such multimode waveguides is of about 25 %, for the horizontal dipole into the fundamental GaAs mode, which is TE-like, and has a major x electric field component. It is worth noting that about 17 % of the dipole emission is coupled to mode 3, which is a third-order TE-like mode. Both modes 1 and 3 are converted into the fundamental Si_3N_4 waveguide TE mode, however, the conversion efficiency is highest ($\approx 69\,\%$) for the fundamental one. Figure S5 shows the fundamental TE-like and TM-like Si_3N_4 waveguide modes, after the mode transformer. The coupling efficiencies from the QD to the these two modes, for the tree dipole configurations, is also displayed. A maximum efficiency of $\approx 13\,\%$ is achieved for the transverse dipole, whereas for the rotating dipole the efficiency is of $\approx 5\,\%$.

We also estimated the coupling efficiency between the Si_3N_4 waveguide and the lensed optical fiber used in our experiments. The manufacturer specification for the lensed fiber was such that it should produce at ≈ 2 µm spot size at its focus, at 980 nm, and so in our simulation, a 2 µm spot-size, horizontally polarized Gaussian beam was launched at the geometrical center of a 685 nm wide and 250 nm tall Si_3N_4 waveguide facet. We note that, in our fabricated devices, the Si_3N_4 waveguides unintendedly made a ≈ 8° angle with respect to the cleaved facet plane. This imperfection was included in our model. An overlap integral was then used to obtain, from the steady-state waveguide field, a coupling ratio of ≈ 23 % into the fundamental TE-like Si_3N_4 mode.

Overall, we expect the QD-lensed fiber coupling efficiency to be of at most $0.23 \times 0.13 \approx 3\,\%$, achieveable with a transverse dipole, for a conservative estimate. We note however that for a rotating dipole, the maximum possible coupling efficiency is estimated to be ≈ 1 %.

Lastly, we note that the maximum QD coupling efficiencies of 26 % and 8 % (in one direction) quoted in the main text for respectively the 400 nm and 800 nm width GaAs waveguides were estimated from simulations of the full geometries as done above, considering only the case of a horizontal dipole radiating inside the GaAs ridge.

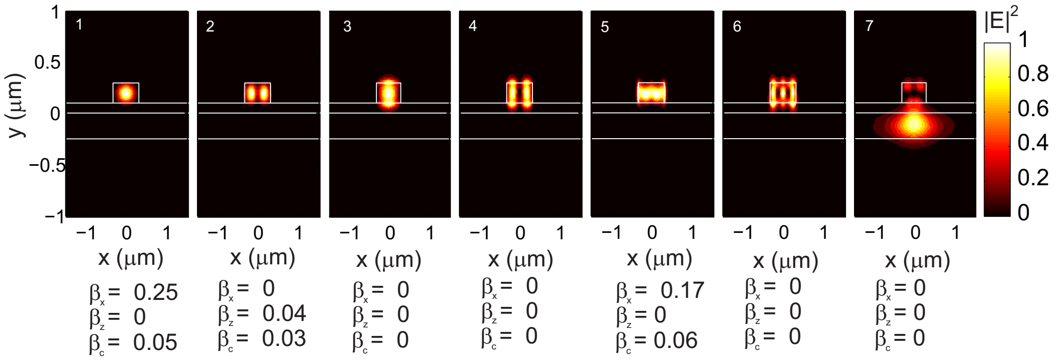

Figure S4: Squared electric field profiles for bound modes of the hybrid nanowaveguide hosting QD 3. Modes 1, 2 and 5 have TE-like character, with major transversal (x) electric field component. Modes 3 and 4 have a TM-like character, with a major x magnetic field component. The $\beta_{x,z,c}$ factors are the coupling between transversal (x), longitudinal (z) or circular (c) dipoles to the corresponding modes.

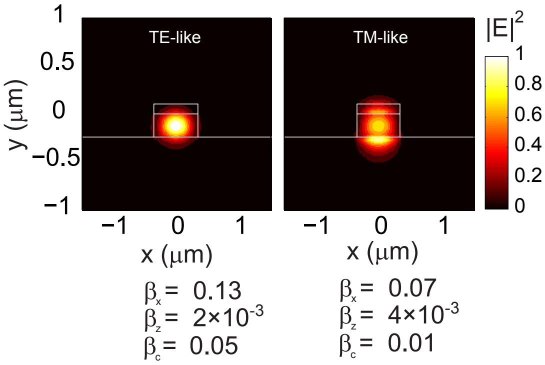

Figure S5: Squared electric field profiles for bound modes of the Si_3N_4 waveguide. Modes 1 and 2 are TE-like and TM-like, respectively. The $\beta_{x,z,c}$ factors are the coupling between transversal (x), longitudinal (z) or circular (c) dipoles to the corresponding modes.

V. Fabry-Perot interferometer evaluation

For the evaluation of the Fabry-Perot-Interferometer (FPI) data, we fit the data with a Voigt[4] (Fig. 4 a) in the main text), Lorentzian (Fig. S6 a)) and Gaussian (Fig. S6 b)) line functions. The Voigt fit gives an R^2 of 0.9884, slightly superior to the Lorentzian and Gaussian ($R^2 = 0.9766$ and $R^2 = 0.9867$, respectively). Inspection of the fits and residuals indicates the Voigt function gives qualitatively better results.

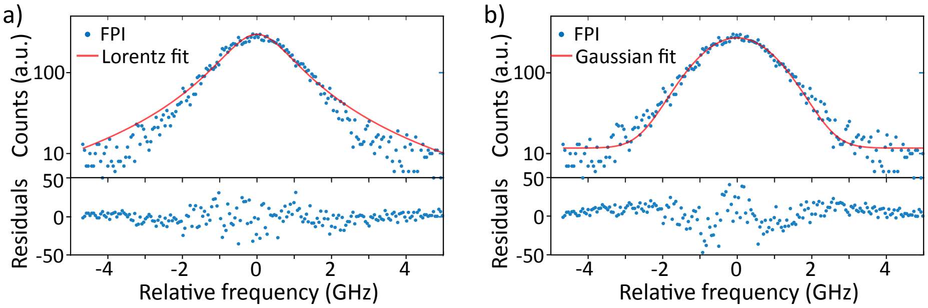

Figure S6: a) FPI data (blue) and Lorentzian fit (red) with residuals. b) FPI data (blue) and Gaussian fit (red) with residuals

VI. Hong-Ou-Mandel setup

In the Hong-Ou-Mandel (HOM) type experiment, the fiber-collected PL was first passed through a $\approx 500\,\mathrm{pm}$ free spectral range fiber-coupled grating filter followed by a long wavelength pass filter, and then guided through quarter- and half-wave plates and a polarization beam splitter (PBS) cube. This was done to bring the polarization of the PL signal into a linear state from an elliptical state that resulted in large part due to scrambling in the non-polarization-maintaining SM collection fiber, though likely also from the inherent polarization of the collected QD emission. The linearly-polarized light was then passed through a half-wave plate and coupled into a polarization-maintaining (PM) fiber PBS. The half-wave plate was aligned to the slow-axis of the fiber PBS, such that the photon stream was maximized at one output port while being suppressed at the other. Throughout the experiment, we could monitor the suppressed polarization output of the fiber PBS at an SNSPD, to verify the long term stability of our polarization filtering system, which could change if the stress on the conventional SM fibers in the setup was accidentally altered. After the fiber-coupled PBS, the QD signal was guided into an unbalanced PM fiber-coupled MZI, with a $\delta\tau \approx 10\,\mathrm{ns}$ arm imbalance. A variable half-wave plate inserted in the long interferometer arm allowed the (linear) polarization of photons travelling through either arm to be, at the second beamsplitter, parallel or orthogonal to each other. We matched the intensity of the photon streams in the two MZI arms by controllably loosening one fiber connection in the short arm, and measured coincidences on the two MZI outputs using the same SNSPDs as in the HBT measurement.

VII. Resonant and phonon-mediated excitation

The coherent excitation of QDs through resonance fluorescence is an important step towards the emission of Fourier-limited photons.[5] In resonance fluorescence, the QD signal needs to be separated from the excitation laser. Waveguide architectures naturally offer spatial separation of pump and detection position, for free-space excitation orthogonal to the wafer. Furthermore, waveguides can act as polarization filters[6] allowing on-chip suppression of pulsed excitation lasers up to a signal-to-noise ratio (SNR) of 40:1.[7] When tuning the excitation laser wavelength close to the QD emission, one can excite the QD through a longitudinal acoustic (LA) phonon-mediated process. Assuming that the LA-phonon mediated and strictly resonant excitation are approximately equally efficient, we use this scheme to probe the QD emission to laser SNR that we can achieve in our system. Applying off-chip polarization filtering as in the HOM experiment and an excitation NA of 0.28, we measure an SNR of about 1:2 as seen in Fig. S7 a). We check the origin of the excess laser signal in our system with two methods. Firstly, we use an excitation NA of 0.1 and repeat the phonon-mediated pumping, losing one order of magnitude in SNR. Secondly, we launch resonant laser light into the Si_3N_4 waveguide at the sample facet, and measure laser light that is scattered into an NA=0.28 towards the top with a conventional CCD camera, see Fig. S7 b). Most of the light is scattered at the GaAs WG taper tips and in the center of the GaAs WG, where the QD is located. Due to time reversal symmetry, we conclude that our current GaAs-Si_3N_4-SiO_2 structure unfortunately scatters large amounts of the top excitation laser into the Si_3N_4 WG, detrimental to laser suppression. With improved waveguide designs, that avoid vertical interfaces near the QD, and a tighter beam focusing reducing the necessary pump powers, higher laser suppression enabling resonance fluorescence from preselected QDs on silicon chips may be possible in the future.

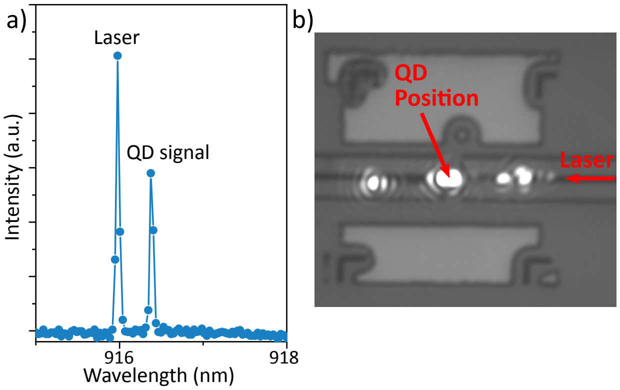

Figure S7: a) µPL spectrum of QD 3 showing the excitation laser and the QD signal in an LA-phonon-assisted excitation (laser excitation from top, detection from side). The laser is suppressed with an SNR of ≈ 1:2. b) Microscope image taken of device QD 3 with moderate white light illumination, while at the same time launching 916.3 nm laser light into the Si_3N_4 WG from the cleaved sample edge. Large amounts of laser are scattered towards the top, as shown by bright white intensity spots. Scattering is particularly strong close to the QD position, and at the GaAs taper tips.

References

(1) Ortner, G.; Yakovlev, D. R.; Bayer, M.; Rudin, S.; Reinecke, T. L.; Fafard, S.; Wasilewski, Z.; Forchel, A. *Physical Review B* **2004**, *70*, 201301.

(2) Davanço, M.; Rakher, M. T.; Schuh, D.; Badolato, A.; Srinivasan, K. *Applied Physics Letters* **2011**, *99*, 041102.

(3) Young, A.; Thijssen, A.; Beggs, D.; Androvitsaneas, P.; Kuipers, L.; Rarity, J.; Hughes, S.; Oulton, R. *Physical Review Letters* **2015**, *115*, 153901.

(4) Abrarov, S.; Quine, B. *Journal of Mathematics Research* **2015**, *7*, p163.

(5) Kuhlmann, A. V.; Prechtel, J. H.; Houel, J.; Ludwig, A.; Reuter, D.; Wieck, A. D.; Warburton, R. J. *Nature Communications* **2015**, *6*, 8204.

(6) Schwartz, M.; Rengstl, U.; Herzog, T.; Paul, M.; Kettler, J.; Portalupi, S. L.; Jetter, M.; Michler, P. *Optics Express* **2016**, *24*, 3089.

(7) Schwartz, M.; Schmidt, E.; Rengstl, U.; Hornung, F.; Hepp, S.; Portalupi, S. L.; llin, K.; Jetter, M.; Siegel, M.; Michler, P. *Nano Letters* **2018**, *18*, 6892–6897.